Clay Minerals, (2013) **48**, 267–276

Microstructural investigation of calcium montmorillonite

M. MATUSEWICZ[1,*], K. PIRKKALAINEN[2], V. LILJESTRÖM[2], J.-P. SUURONEN[2], A. ROOT[3], A. MUURINEN[1], R. SERIMAA[2] AND M. OLIN[1]

[1] *VTT Technical Research Centre of Finland, P.O. Box 1000, FI-02044 VTT, Finland,* [2] *Department of Physics, University of Helsinki, P.O. Box 64, FI-00014 University of Helsinki, Finland, and* [3] *MagSol, Tuhkanummenkuja 2, FI-00970 Helsinki, Finland*

(*Received 4 December 2012; revised 31 March 2013; Editor: John Adams)*)

ABSTRACT: Bentonite clay is planned to form a part of deep-geological repositories of spent nuclear fuel in several countries. The extremely long operation time of the repository requires an in-depth understanding of the structure and properties of used materials. In this work the microstructure of a simplified system of Ca-montmorillonite is investigated using a set of complementary methods: X-ray diffraction, small angle X-ray scattering, nuclear magnetic resonance, transmission electron microscopy and ion exclusion. The paper presents experimental results obtained from compacted, water saturated samples in the dry density range 0.6–1.5 g/cm^3. It can be observed that different methods yield similar quantification of water present in the interlamellar space. Combined results support the multiple porosity concept of the bentonite structure.

KEYWORDS: HLW repositories, bentonite buffer, microstructure, montmorillonite, calcium.

MX-80 bentonite is planned to be used as a part of the engineered barrier system in the high-level nuclear waste repository in Finland (Posiva, 2010). A thorough understanding of the material is needed to provide a sound scientific basis for modelling of the repository performance. Currently, two different conceptual models are used to predict bentonite behaviour (Savage, 2012). The "single porosity model" treats clay as a bentonite–pore water system controlled by ion equilibria phenomena with all water present in one type of porosity (Birgersson & Karnland, 2009). The "multiple porosity model" (Kozaki *et al.*, 2001; Bradbury & Baeyens, 2002; Carlsson *et al.*, 2012; Muurinen, 2009; Holmboe *et al.*, 2012) distinguishes two main groups of water: one present in the interlamellar space and the other in the volume between clay stacks.

* E-mail: michal.matusewicz@vtt.fi
DOI: 10.1180/claymin.2013.048.2.08

The multiple porosity model thus takes into account the heterogeneous nanostructure of clays. Montmorillonite is the main mineral component of MX-80 bentonite. Montmorillonite consists of negatively charged clay layers which form lamellar stacks of different sizes (e.g. Segad *et al.*, 2012). The charge of the clay layers is compensated by counter ions present close to the lamellar surfaces. Between the stacks there are larger pore structures where smaller stacks and single, delaminated clay platelets may be found.

In this study an attempt was made to characterize the clay microstructure. Pure homoionic montmorillonite can be considered as a simplified system providing relevant information on the behaviour of natural bentonite. We have used a set of complementary methods to study Ca-montmorillonite structure. Three of them, X-ray diffraction and small angle X-ray scattering (XRD and SAXS), nuclear magnetic resonance (NMR) and ion exclusion (IE), provide averaged and indirect information that can be used to verify assumed

structure concepts. In addition, we use transmission electron microscopy (TEM) to obtain qualitative images of the clay system over a wide range of magnifications.

MATERIALS AND METHODS

Ca-montmorillonite

The clay used in this study was montmorillonite obtained from MX-80 bentonite by the purification method used by Tributh & Lagaly (1986) and changing the exchangeable cations to calcium ions. Samples were prepared by uniaxial compaction of air-dry clay to cylindrical, stainless steel equilibration cells. Clay was compacted to dry densities ranging from 0.6 to 1.5 g/cm^3. Montmorillonite pellets, 1 cm in height, 2 cm in diameter, were confined between stainless steel filters of 2 μm pore size allowing contact with an external liquid, i.e. either MilliQ water or 0.1 M $Ca(ClO_4)_2$. Equilibration time was between 5 to 12 months. Investigated samples are listed in Table 1.

Ion exclusion

Dried clay samples from the experiment were dispersed in a known amount of water and centrifuged. The concentration of perchlorate ions in the supernatant was measured using an ion selective electrode (Nico 2000). The fraction of the total sample volume, for which the measured amount of perchlorate would give concentration equal to the equilibrating solution, is referred to as perchlorate porosity.

It was assumed that perchlorate anions do not enter into the interlamellar pores and are excluded from a volume close to the clay surface (Kozaki *et al.*, 2001). Anion exclusion was used to estimate the amount of water present in the interlamellar pores. Using average interlamellar distances from X-ray diffraction, the surface area of the interlamellar pores was calculated. By comparison with the specific surface area of montmorillonite (750 m^2/g, Sposito & Prost, 1982; Eslinger & Peaver, 1988) estimation of the average number of platelets forming a stack was possible.

X-ray diffraction and small angle X-ray scattering

From the water-saturated pellet a cylindrical subsample (4 mm in diameter) was cut perpendicularly to the compaction axis and cut into 0.3–0.5 mm slices. Slices were placed in metal rings closed tightly by a thin plastic film. The whole preparation process was conducted in the glove box with relative humidity around 80%. The as-prepared samples were characterized using X-ray scattering.

The X-rays were generated using a conventional sealed X-ray tube with Cu-anode (PANalytica, Almelo, the Netherlands). The X-ray beam was collimated and monochromated to Cu-$K\alpha$ radiation (wavelength 1.54 Å) using a Montel-multilayer mirror. The scattered intensity was collected using a Bruker Hi-Star area detector.

The X-ray scattering patterns of the samples were measured with two different sample-to-detector distances (17.6 cm and 59.7 cm), corresponding to magnitudes of the scattering vector $q = 4\pi\sin(\theta/\lambda)$ (where λ is the wavelength of the radiation and θ is the Bragg angle) of 0.065 Å^{-1} to 1.1 Å^{-1} (low-angle X-ray diffraction) and 0.021 Å^{-1} to 0.39 Å^{-1} (small-angle X-ray scattering). The q range was calibrated using a silver behenate standard sample (Huang *et al.*, 1993). The 2D intensity patterns were spherically averaged and corrected for absorption, air scattering and detector geometry. In the case of the low-angle X-ray diffraction patterns, the Lorentz-Polarization correction for randomly oriented powder was also applied (Moore & Reynolds, 1997).

The maximum volume of interlamellar pores was calculated by multiplying the interlamellar distance

TABLE 1. Summary of the samples used in the experiments.

Sample name	C5	D1	D3	D5	C6	D2	D4	D6
Dry density (g/cm^3)	1.41	1.22	0.94	0.65	1.45	1.22	0.98	0.63
Bulk density (g/cm^3)	1.90	1.78	1.60	1.42	1.93	1.78	1.63	1.41
Solution	MiliQ water				0.1 M $Ca(ClO_4)_2$			

obtained from X-ray diffraction by the specific surface area of montmorillonite. This was assumed to be the interlamellar porosity, and the remaining water of the total water content was assumed to be in the pores between clay stacks.

The low-angle diffraction patterns included the basal Bragg reflections from planes (001), (002) and (003) of the montmorillonite crystal structure (Viani *et al.*, 2002). The positions of these reflections are related to the average basal spacings *d*, the intensities to the position of scatterers (e.g. atoms or molecules) inside the unit cell, and the breadths to the distribution of the size of coherent scattering domains (CSDs) (Moore & Reynolds, 1997; Plançon, 2002). In the case of smectites such as montmorillonite, the basal spacings vary depending on the number of layers of water molecules in the interlayers (Ferrage *et al.*, 2005). In addition to these, the position and shape of the reflections are also affected by disorder in the crystalline phase. One type of disorder is interstratification, where several different basal spacings co-exist within the crystallites due to different amounts of water monolayers in interlayers. Interstratification is known to shift the reflections from the ideal positions given by the relationship $q = 2\pi/d_{001}$ and contributes to the asymmetric tails of the reflections (Holmboe *et al.*, 2012; Ferrage *et al.*, 2010).

The low-angle scattering patterns were used for determination of average basal spacing and the mean stack size of CSDs. In the cases where all the three basal reflections were observed, the average basal spacing was determined by plotting the reflection positions as a function of reflection order *l*, and by fitting a line which intersects the *x* axis at zero (the position of the 00l reflection is $q_{00l} = 2\pi l/d_{00l}$). The average basal spacing was then calculated from the slope of the fit, giving a more reliable value than by simply calculating the basal spacing from the position of 001 reflection. In some cases, only the 001 reflection was seen and the average basal spacing was estimated from its position.

The average size of the montmorillonite crystallites (CSDs) in the [00l] direction was estimated from the reflection breadths using an assumption that reflection line broadening arises from both small particle size and strain broadening (Williamson & Hall, 1953) and can be given as a sum of the well-known Scherrer equation (Moore & Reynolds, 1997) and strain dependent part $\varepsilon C \tan(\theta)$, where ε is the crystal strain, C is a constant and θ is the Bragg angle of the reflection. By multiplication with $\cos(\theta)$ the line breadth can be given as

$$\Delta(2\theta)\cos(\theta) = (K\lambda)/B + \varepsilon C \sin(\theta)$$

where $\Delta(2\theta)$ is the full widths at half maximum (FWHM) of the reflection, K is the Scherrer constant (0.9) and *B* is the size of the CSD. By determining the FWHMs of several reflection orders and fitting a line to the Williamson-Hall plot ($\sin(\theta)$, $\Delta(2\theta)\cos(\theta)$), the mean CSD size can be calculated from the intercept of the fit and the first term on the right in the previous equation. The FWHM from all observed reflections was determined and the respective size of CSDs was calculated using the Scherrer equation and from the Williamson-Hall plot when more than one reflection was seen. The reflection broadening due to the instrument was omitted, and thus the calculated CSD sizes are slightly underestimated. The mean number of basal repeat units (stack size), *N*, was calculated by dividing the mean CSD size by the average basal spacing.

The small angle X-ray scattering intensity curves were used to determine the average basal spacing, the size distribution of basal repeat units (stack sizes) in CSDs and estimate the volume fraction of the different basal spacings present. The intensity curves were fitted to a one-dimensional diffraction grating model similar to the one used by Pizzey *et al.* (2004) and van Duijneveldt *et al.* (2005) in their study on clay colloids, but with modifications to account for stacks with different basal spacings. The model is the same as equation 3 in Muurinen (2009) with the difference that only two different basal spacings are taken into account, with one being the hydrate state nearest to the average basal spacing calculated from the 001 reflection, the other being the nearest neighbour hydrate state with larger basal spacing. This was done in order to take into account the asymmetric tail of the 001 reflection towards lower *q* values due to e.g. interstratification. The statistics assumed for the stack size distribution is assumed to be a sum of Poisson distribution and a box distribution as proposed by Hermes *et al.* (2006). The box distribution is fixed to $N = 1$ to represent the single delaminated platelets and the Poisson distribution has a mean value $N > 1$ to represent polydispersivity of stack sizes. The relative amount of delaminated platelets to laminated stacks is taken into account as a weighting the sum of box and

Poisson distributions. The determined average stack size N_{SAXS} is the best fit value for the mean value of the Poisson distribution. Instrumental broadening of reflections was omitted, and thus the calculated stack sizes are slightly underestimated. In the model used the "hard phase" thickness was fixed to 9.5 Å as proposed by Muurinen (2009). This value corresponds to the basal spacing of dehydrated montmorillonite. The electron density contrast between CSDs and its surroundings is taken into account with parameter φ which governs the scattered intensity of the zero-order peak (Pizzey *et al.*, 2004; Muurinen, 2009). When φ is zero, the zero-order peak will have full intensity, and when φ is one, the zero-order peak will have zero intensity. The power law region at lower q values was not included in the fits, and was only examined qualitatively.

NMR

From the water-saturated pellet, a cylindrical subsample was probed along the compaction axis. The same cylindrical cutter was used as in the preparation of the X-ray scattering specimen, but the whole subsample was immediately transferred into a glass tube closed tightly by PTFE corks. The measurements were carried out with a high-field Chemagnetics CMX Infinity 270 MHz NMR spectrometer using a spin-locking CPMG (Carr-Purcell-Meiboom-Gill) technique (Santyr *et al.*, 1988). Briefly, this means that measured signal decays are associated with the rotating-frame spin-lattice relaxation time, $T_{1\rho}$. This was confirmed by carrying out equivalent traditional $T_{1\rho}$ experiments on some samples to check that the same signal decay was obtained. The use of the CPMG method to measure $T_{1\rho}$ is advantageous, since the whole decay signal can be obtained in one shot and a finer resolution of the decay can be obtained for a given time. It is possible that $T_{1\rho}$ and T_2 are equivalent here, but it is unlikely we are measuring T_2 with such a short refocusing delay (22 μs). The measurement of $T_{1\rho}$ necessitates that all CPMG measurements are carried out with the same inter-pulse spacing τ in order to allow proper comparisons (same spin-locking field) between results from different samples. To conclude, this study utilised ^{1}H NMR $T_{1\rho}$ relaxation time measurements using the short inter-pulse CPMG method. The time used between the centre of the 180º pulses, τ, was 22 μs in all cases (equivalent to a 22.7 kHz spin locking field). The software package XPfit (SoftScientific,) was used to fit a distribution of exponential decays to the decay curves obtained from the NMR measurements. The sample temperature was kept at 23ºC by gas flushing.

The observed overall NMR decay signal is given as:

$$M = \sum_{1}^{n} M_{0,i} \exp\left[\frac{-t}{T_{1\rho,i}}\right]$$

where M is the spin locked macroscopic magnetization vector, M_0 is the value of M at equilibrium, t is time, and $T_{1\rho}$ is the spin-lattice relaxation time in the rotating frame associated with decay i.

Since water in smaller pores interacts more with the paramagnetic Fe^{3+} than that in larger pores, the decays with the shorter relaxation time should be associated with the IL water and longer decays with the non-IL water. It should be stressed that it is not *a priori* possible to tell how many relaxation processes are needed to fit the observed curve.

The software XPfit was used to fit a broad distribution of exponential decay times and an arbitrary "cut-off" time (510 μs) was chosen (to match the results from the other methods) below which it was assumed that decay signals shorter than this cut-off were due to water in smaller pores associated with IL water. Remaining water was assumed to be outside of the interlamellar pores.

TEM

Samples for electron microscope imaging were prepared from the water-saturated, compacted state using high-pressure freezing (Studer *et al.*, 2001, Holzer *et al.*, 2010). Samples ~0.2 mm thick and 1 mm in diameter were placed in the freezing vessels and frozen using a Leica EM Pact machine. Subsequently, samples were subjected to a freeze substitution process and embedded in Epon resin. Sections of 90 nm thickness were prepared with an ultramicrotome and imaged with an FEI Tecnai 12 microscope at a working voltage of 120 kV. Micrographs were processed by using ImageJ (Schneider *et al.*, 2012) and GIMP software.

RESULTS

X-ray scattering results

The results of low angle X-ray diffraction are given in Tables 2 and 3. The diffraction patterns are

TABLE 2. Results from low-angle X-ray diffraction for samples in water. For each dry density the determined values are shown for the average basal spacing *d*, the corresponding dominant hydration layer type and the mean number of basal repeat units calculated from three first basal reflections and from the Williamson-Hall plot. The 2σ confidence bounds for determined values are given in parenthesis where applicable.

Dry density (g/cm^3)	*d* (nm)	Hydrate	N_{001}	N_{002}	N_{003}	$N_{W\text{-}H}$
0.65	1.94 (0.04)	3W	5.9	4.7	5.0	6.1**
0.94	1.93 (0.03)	3W	6.4	5.4	5.8	6.4**
1.22	1.91 (0.03)	3W	6.0	5.2	5.3	6.3**
1.48*	1.60 (0.2)	2W	6.1	–	–	–

* Only one basal reflection was observed. **The fit to Williamson-Hall plot was unreliable.

shown in Fig. 1 as a function of basal spacing $d = 2\pi/q$ and compared to the upper and lower bound of basal spacings for 1W, 2W, 3W and 4W hydration layer types given in literature (Holmboe *et al.*, 2012).

The results from SAXS intensity curve fitting are shown in Tables 4 and 5. The intensity curves and the corresponding model best fits are shown in Fig. 2.

Stacking

The average number of clay layers per stack calculated on the basis of anion exclusion is presented in Table 6. A clear increase of the stack size with the increase of sample density is observed.

Porosity

The volume fractions of interlamellar pores obtained from X-ray scattering, NMR and ion exclusion results are plotted in Fig. 3. All the values show a similar trend of proportional increase of interlamellar porosity with an increase of sample density. For the densities around 1.5 g/cm^3 interlamellar porosity approaches the theoretical total porosity value, reaching the total porosity in case of the NMR estimation.

TEM imaging

Transmission electron microscopy gives the qualitative image of the heterogeneous clay structure. In the micrographs various microstructural features as μm-sized pores, low and medium density clay and dense stacks of montmorillonite layers can be seen (Fig. 4).

DISCUSSION

The model of the montmorillonite clay structure described in the introduction corresponds well to

TABLE 3. Results from low-angle X-ray diffraction for samples in Ca-perchlorate solution. For each dry density the determined values are shown for average basal spacing *d*, the corresponding dominant hydration layer type and the mean number of basal repeat units calculated from three first basal reflections and from the Williamson-Hall plot. The 2σ confidence bounds for determined values are given in parenthesis where applicable.

Dry density (g/cm^3)	*d* (nm)	Hydrate	N_{001}	N_{002}	N_{003}	$N_{W\text{-}H}$
0.63	1.91 (0.01)	3W	7.2	6.7	6	8.0 (1.4)
0.98	1.92 (0.02)	3W	7.0	6.4	5.8	7.9 (0.9)
1.22	1.90 (0.02)	3W	6.1	5.6	4.8	6.1 (3.2)
1.52*	1.58 (0.05)	2W	7.4	–	–	–

* Only one basal reflection was observed.

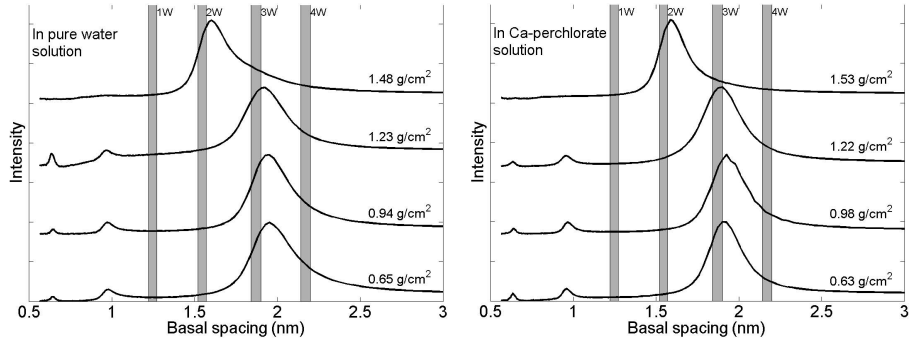

FIG. 1. The low-angle X-ray diffraction patterns of samples in water (left) and Ca-perchlorate solution (right) as a function of basal spacing. The upper and lower bounds for literature values given for 1W, 2W, 3W and 4W hydrates of montmorillonite are shown in grey.

the image provided by the transmission electron microscopy. Careful inspection of micrographs clearly shows highly complicated and heterogenous systems. The presence of clay layers in stacks of different size, pores of various shapes and volumes can be confirmed. However, one should bear in mind the influence of sample preparation on the sample appearance. The preparation process is performed on extremely small samples and requires introducing to the clay pore space a liquid of different electric constant. We observe a slight decrease of the interlamellar distance, possibly due to the sample drying. In the interpretation of the micrographs of high resolution one should remember that the image is in fact a shadowgram of the 90 nm thin section.

According to low-angle diffraction and SAXS results (Tables 2, 3, 4 and 5), the dominant hydration layer type of montmorillonite crystallites for dry densities between 0.63 to 1.23 g/cm^3 was 3W, with average basal spacings close to 1.9 nm. The slightly asymmetric shape of the low-angle diffraction maxima and SAXS model fitting implied that the montmorillonite prepared in pure water is slightly 3W-4W interstratified. Such interstratification was also observed for the montmorillonite prepared in Ca-perchlorate solution but to a lesser degree. The data analysis methods used were not capable of quantifying interstratification accurately, but the effect of interstratification can be seen from Fig. 1; the first-order basal reflection (001) does not peak exactly at the positions given in literature for 1W, 2W, 3W or 4W hydrate types (Holmboe *et al.*, 2012).

The most distinctive feature of the series of low-angle diffraction intensities (Figs 1 and 2) for the

TABLE 4. Results from small-angle X-ray scattering for samples in water. For each dry density the determined values are shown for average basal spacing d_1 of the most dominant hydration layer type and its estimated volume fraction p_1. Corresponding values are given for the nearest neighbour hydration layer type d_2 and p_2 with higher basal spacing than the dominant type. The average stack size is N_{SAXS} and the electron density contrast between stacks and surroundings represented by the φ parameter.

Dry density (g/cm^3)	d_1 (nm)	p_1 (%)	d_2 (nm)	p_2	N_{SAXS}	φ
0.65	1.94 (0.02)	87.8	2.22 (0.05)	12.2	5.5 (0.1)	0.19
0.94	1.92 (0.02)	88.9	2.17 (0.05)	11.1	6.6 (0.2)	0.37
1.23	1.90 (0.02)	90.4	2.13 (0.05)	9.6	7.0 (0.2)	0.58
1.48*	1.64 (0.06)	77.9	1.89 (0.02)	22.1	5.9 (0.7)	0.70

* The 001 reflection was not fully observed.

TABLE 5. Results from small-angle X-ray scattering for samples in Ca-perchlorate solution. For each dry density the determined values are shown for average basal spacing d_1 of the most dominant hydration layer type and its estimated volume fraction p_1. Corresponding values are given for the nearest neighbour hydration layer type d_2 and p_2 with higher basal spacing than the dominant type. The average stack size is N_{SAXS} and the electron density contrast between stacks and surroundings represented by the φ-parameter.

Dry density (g/cm^3)	d_1 (nm)	p_1 (%)	d_2 (nm)	P_2	N_{SAXS}	φ
0.63	1.90 (0.02)	92.4	2.13 (0.05)	7.6	7.5 (0.2)	0.13
0.98	1.91 (0.02)	91.5	2.16 (0.05)	8.5	6.8 (0.2)	0.32
1.22	1.91 (0.02)	93.7	2.14 (0.05)	6.3	6.1 (0.2)	0.61
1.53*	1.64 (0.06)	85.4	1.88 (0.02)	14.6	6.5 (0.7)	0.68

* The 001 reflection was not fully observed.

highest dry density samples (1.48 and 1.53 g/cm^3) was the change of the position of the first-order intensity maximum (001) and the disappearance of the second-order intensity maximum (002). The shift in (001) was of course observed in the respective SAXS patterns as well. The shift in the peak position can be explained by the removal of one layer of water molecules from the interlayers of montmorillonite crystallites. Thus, the most dominant hydration layer type in these samples was 2W, with an average basal spacing close to 1.6 nm. The disappearance of the 002 reflection was probably due to significant interstratification of hydration types 2W and 3W. The third-order maximum (003) for the 2W hydrate type was outside the q range seen with the experiment.

The results for the average stack size indicated that the size of the CSDs does not change as a function of dry density. According to both low-angle X-ray diffraction and SAXS, the CSD size was around 6 to 8 platelets per stack. The montmorillonite prepared in Ca-perchlorate solution had a slightly higher CSD size, but this result could also arise from the inability of the methods used to accurately take into account peak broadening due to interstratification.

At small q values the intensity shows power law behaviour approximately corresponding to scattering from platelets (Glatter & Kratky, 1982). The slope is steeper for low density samples than for high density samples (Fig. 2). The SAXS model used does not fit to the experimental intensity well in this region. This is due to interparticle scattering, which is not taken into account in the present model. The differences in the slope steepness can be explained by the electron density contrast between the clay platelets and their surroundings: in low dry density samples the electron density contrast is high, because water fills the spaces between the stacks, and therefore full scattering in the low q region is observed. In the

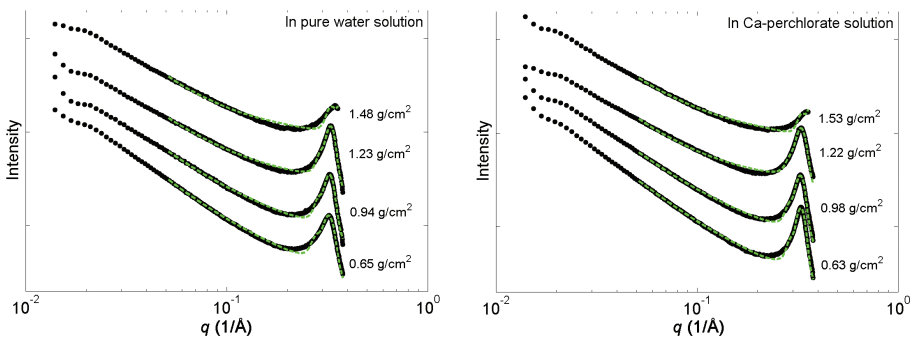

FIG. 2. The small-angle scattering patterns of samples in water (left) and Ca-perchlorate solution (right) as a function of magnitude of scattering vector q. The green dashed line is the best fit from SAXS modelling.

TABLE 6. Values of stacking number calculated from IE.

Sample name	C6	D2	D4	D6
Layers per stack	21	9	5	3

samples with high dry density the distance between the clay stacks is smaller, and thus the electron density contrast is also reduced, resulting in less scattering intensity at low q values. The decrease in electron density contrast as a function of dry density can be seen in the increase in φ parameter (Tables 4 and 5).

The methods used to interpret the low-angle diffraction and SAXS patterns were unable to fully take into account the interstratification clearly present in the montmorillonite. The effect of interstratification was most clearly seen in the two highest dry density samples, where the first-order basal reflection was significantly asymmetric and the second-order basal reflection was entirely suppressed. This prevented the accurate determination of average basal spacings and stack sizes from low-angle X-ray diffraction and the SAXS model used was not able to reproduce the first order basal reflection shape very well. Several more advanced X-ray diffraction models are available for full diffraction pattern modelling, where disorder such as interstratification is taken into account (Plançon, 2000; Ferrage *et al.*, 2010; Holmboe *et al.*, 2012). In the lower dry density samples, interstratification is present, but to a much lower degree. In these cases, the methods used were sufficient to explain the features in low angle x-ray diffraction and SAXS.

The average stack sizes obtained from XRD, SAXS and IE results were compared. The first two showed a constant stacking number with the increase of density; the second indicated clear increase of the size of stacks with the increase of sample density. Both approaches yielded very similar results in the low density area. The increase of an IE-based stacking number at high densities can be intuitively explained by describing two stacks parallel to one another and separated by disordered, misaligned platelets. In the dense system the distance between disordered platelets can be small enough to exclude perchlorate ions from penetrating between them, whereas in the low-density system anions would be able to penetrate larger pores between the disordered platelets. X-ray scattering based estimation of the average stack size would give the same result in both cases.

A broad distribution of relaxation times was found in the NMR studies which gradually shifted to lower average times with higher density, indicating a reduction in general domain size. This can mean that the domain sizes present are spread over a narrow range which cannot be distinguished by NMR. In that case, the cut-off method used here, and elsewhere (Ohkubo *et al.*, 2008), is the only way to separate the interlamellar (IL) and non-interlamellar (non-IL) water. It could also mean that there are quite different domain sizes with very different relaxation times, but exchange

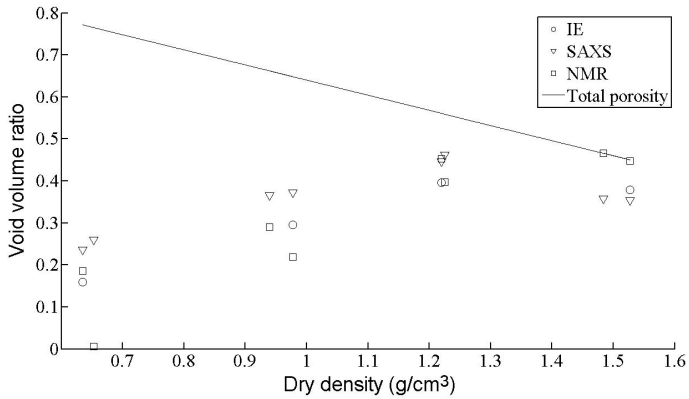

FIG. 3. The volume fractions of interlamellar pores obtained from IE, X-ray scattering and NMR. Solid line depicts the total water porosity of the system.

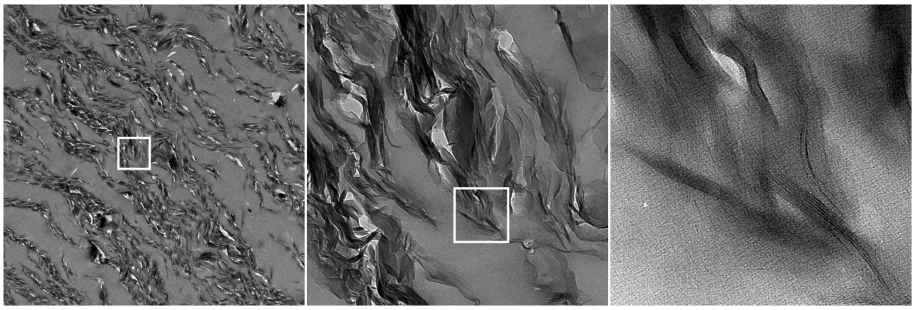

FIG. 4. TEM micrographs of sample D6. The edge of the left picture is 10 μm, central 1 um and right 175 nm. White frames in the left and central image correspond to the area shown in the central and right picture correspondingly.

of the water between IL and non-IL domains is fast enough to average the relaxation times to one broad range. Given the other evidence here, it seems likely that the differences between the IL domain size and the non-IL domain size is not so great, so we favour the first explanation of the broad distribution of the relaxation times. Interestingly, at the lowest density, we do in fact see separated definable relaxation components, but only for the samples with the perchlorate anion. We speculate that at low densities, there may also be water in the samples in macropores which are generally in fast exchange with all the other domains (all water is considered non-IL), except when the large perchlorate anion is present. Presumably the anion in this case can slow down the fast exchange by holding some water more tightly in the hydration shell. This would also explain why one of the NMR data points (for the water sample at low density) gives too low a value for the IL water.

Estimation of interlamellar porosity using different methods gave results that agreed well, although all the methods have limitations. Investigation of the sample taken out from the equilibration cell does not fully correspond to the *in situ* investigation. The estimation based on X-ray scattering relies on the average interlamellar distance and the specific surface area, but only a fraction of the total surface area can be counted as the interlamellar surface. This results in an overestimation of the interlamellar volume. On the other hand the IE volume was computed assuming total exclusion from the interlayer pores, but also some volume close to the external surfaces of stacks and delaminated platelets is inaccessible for anions. Finally, the NMR approach using relaxation time has been scaled on the basis of the X-ray scattering and IE methods. However, the relation between the relaxation time and pore size gives this method a sound scientific basis. Combining results of X-ray scattering and IE allows the estimation of the fraction of clay forming stacks and applying this information reduces the error in the interlamellar volume calculation.

Combining X-ray scattering, IE, NMR and TEM provides a view on the structure of compacted, water-saturated Ca-montmorillonite. The data obtained, apart from the NRM results at high density, support the multiple porosity model by bringing the evidence of a large proportion of water in the sample being present in the narrow slit-like pores between the clay layers. Further work is planned to apply methods described in this article to sodium montmorillonite and MX-80 bentonite.

ACKNOWLEDGMENTS

The research leading to these results has received funding from The European Atomic Energy Community's Seventh Framework Programme (FP7/2007–2011) under grant agreement nº295487 (the BELBaR project) and Finnish Research Programme on Nuclear Waste Management (KYT) 2011-2014 (BOA project). Financial support from the VTT Graduate School is acknowledged (M.M.). K.P. gratefully thanks the Magnus Ehrnrooth foundation for research funding (grant FY2012n39). TEM imaging was carried out in the EM Unit of the Institute of Biotechnology at Helsinki University. The suggestions and comments of referees are greatly acknowledged.

REFERENCES

Birgersson M. & Karnland O. (2009) Ion equilibrium between montmorillonite interlayer space and an external solution – consequences for diffusional

transport. *Geochimica et Cosmochimica Acta*, **73**, 1908–1923.

Bradbury M.H. & Baeyens B. (2002) Porewater chemistry in compacted re-saturated MX-80 bentonite: Physico-chemical characterisation and geochemical modelling. PSI Bericht Nr. 02-10. Paul Sherrer Institut, Villigen, Switzerland.

Carlsson T., Muurinen A., Matusewicz M. & Root A. (2012) Porewater in compacted water-saturated MX-80 bentonite. Pp. 397-402 in: *MRS Proceedings* (R.M. Carranza, G.S. Duffo & R.B. Rebak, editors). Cambridge University Press. New York. Vol. 1475. ISBN 978-1-60511-452-1.

Eslinger E. & Peaver D. (1988) *Clay Minerals for Petroleum Geologists and Engineers.* Illustrated edition. SEPM, Tulsa, USA.

Ferrage E., Lanson B., Malikova N., Plançon A., Sakharov B.A. & Drits V.A. (2005) New insights on the distribution of interlayer water in bi-hydrated smectite from X-ray diffraction profile modeling of 001 reflections. *Chemistry of Materials*, **17**, 3499–3512.

Ferrage E., Lanson B., Michot L.J. & Robert J. (2010) Hydration properties and interlayer organization of water and ions in synthetic Na-smectite with tetrahedral layer charge. Part 1. Results from X-ray diffraction profile modeling. *The Journal of Physical Chemistry C*, **114**, 4515–4526.

Glatter O. & Kratky O. (1982) *Small Angle X-ray Scattering*. London: Academic Press.

Hermes H.E., Frielinghaus H., Pyckhout-Hintzen W. & Richter D. (2006) Quantitative analysis of small angle neutron scattering data from montmorillonite dispersions. *Polymer*, **47**, 2147–2155.

Holmboe M., Wold S. & Jonsson M. (2012) Porosity investigation of compacted bentonite using XRD profile modeling. *Journal of Contaminant Hydrology*, **128**, 19–32.

Holzer L., Münch B., Rizzi M., Wepf R., Marschall P. & Graule T. (2010) 3D-microstructure analysis of hydrated bentonite with cryo-stabilized pore water. *Applied Clay Science*, **47**, 330–342.

Huang T.C., Toraya H., Blanton T.N. & Wu Y. (1993) X-ray powder diffraction analysis of silver behenate, a possible low-angle diffraction standard. *Journal of Applied Crystallography*, **26**, 180–184.

Kozaki T., Inada K., Sato S. & Ohashi H. (2001) Diffusion mechanism of chloride ions in sodium montmorillonite. *Journal of Contaminant Hydrology*, **47**, 159–170.

Moore D.M. & Reynolds R.C. (1997) *X-ray Diffraction and the Identification and Analysis of Clay Minerals.* Oxford University Press.

Muurinen A. (2009) *Studies on the Chemical Conditions and Microstructure in the Reference Bentonites of Alternative Buffer Materials Project (ABM) in Äspö. 2009-42.* Posiva OY, Eurajoki. 46 pp.

Ohkubo T., Kikuchi H. & Yamaguchi M. (2008) An approach of NMR relaxometry for understanding water in saturated compacted bentonite. *Physics and Chemistry of the Earth, Parts A/B/C*, **33**, Supplement 1, S169–S176.

Pizzey C., Klein S., Leach E., van Duijneveldt J.S. & Richardson R.M. (2004) Suspensions of colloidal plates in a nematic liquid crystal: a small angle x-ray scattering study. *Journal of Physics: Condensed Matter*, **16**, 2479–2496.

Plançon A. (2002) New modeling of X-ray diffraction by disordered lamellar structures, such as phyllosilicates. *American Mineralogist*, **87**, 1672–1677.

Posiva (2010) *Nuclear Waste Management at Olkiluoto and Loviisa Power Plants: Review of Current Status and Future Plans for 2010-2012.* TKS-2009, Posiva OY, Eurajoki.

Santyr G.E., Henkelman R.M. & Bronskill M.J. (1988) Variation in measured transverse relaxation in tissue resulting from spin locking with the CPMG sequence. *Journal of Magnetic Resonance*, **79**, 28–44.

Savage D. (2012) *Prospects for Coupled Modelling.* STUK-TR 13, STUK Radiation and Nuclear Safety Authority, Helsinki, Finland.

Schneider C.A., Rasband W.S. & Eliceiri K.W. (2012) NIH Image to ImageJ: 25 years of image analysis. *Nature Methods*, **9**, 671–675.

Segad M., Hanski S., Olsson U., Ruokolainen J., Åkesson T. & Jönsson B. (2012) Microstructural and swelling properties of Ca and Na montmorillonite: (in situ) observations with Cryo-TEM and SAXS. *The Journal of Physical Chemistry C*, **116**, 7596–7601.

SoftScientific, http://www.softscientific.com/science/xpfit.html.

Sposito G. & Prost R. (1982) Structure of water adsorbed on smectites. *Chemical Reviews*, **82**, 553–573.

Studer D., Graber W., Al-Amoudi A. & Eggli P. (2001) A new approach for cryofixation by high-pressure freezing. *Journal of Microscopy*, **203**, 285–294.

Tributh H. & Lagaly G. (1986) Aufbereitung und Identifizierung von Boden- und Lagerstättentonen. I. Aufbereitung der Proben im Labor. *GIT-Fachzeitschrift für das Laboratorium*, **30**, 524–529.

van Duijneveldt J.S., Klein S., Leach E., Pizzey C. & Richardson R.M. (2005) Large scale structures in liquid crystal/clay colloids. *Journal of Physics: Condensed Matter*, **17**, 2255.

Viani A., Gualtieri A.F. & Artioli G. (2002) The nature of disorder in montmorillonite by simulation of X-ray powder patterns. *American Mineralogist*, **87**, 966–975.

Williamson G.K. & Hall W.H. (1953) X-ray line broadening from filed aluminium and wolfram. *Acta Metallurgica*, **1**, 22–31.